ACS OMEGA

Article

Cite This: ACS Omega 2018, 3, 6880−6887

Combination of Solid-State and Electrochemical Impedance Spectroscopy To Explore Effects of Porosity in Sol−Gel-Derived $BaTiO_3$ Thin Films

Joshua Whittam,[†] Andrew L. Hector,*[,†] Christopher Kavanagh,[‡] John R. Owen,[†] and Gillian Reid[†]

[†]Chemistry, University of Southampton, Highfield, Southampton SO17 1BJ, U.K.

[‡]Deregallera Ltd, Unit 2 De Clare Court, Pontygwindy Industrial Estate, Caerphilly CF83 3HU, U.K.

Supporting Information

ABSTRACT: $BaTiO_3$ thin films were deposited onto polycrystalline Pt using a dip-coating technique, with annealing temperatures of 750−900 °C. To avoid film imperfections such as cracking or pinholes, key conditions, including aging periods, water content, and stirring speeds, were refined to produce a pinhole-free, uniform film with some porosity. Whereas those coated a single time short circuited during electrical characterization, this could be avoided in films produced by multiple coating cycles. The effective permittivity of a 600 nm $BaTiO_3$ film was measured at 290 by fitting solid-state impedance data in the frequency range of 100 Hz to 1 MHz. Electrochemical impedance with an aqueous electrolyte allowed evaluation of the porosity, which remained fairly constant between 1 and 5 coating cycles. Using this method, it was possible to estimate the effective permittivity of the $BaTiO_3$ itself as 374 and hence to evaluate the increase in the effective permittivity that could be achieved by minimizing porosity.

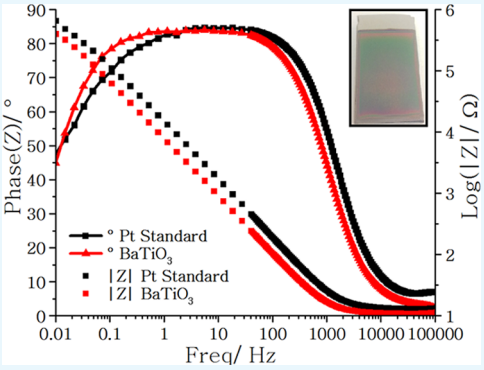

INTRODUCTION

Titanate perovskites such as lead zirconate titanate ($PbZr_xTi_{1-x}O_3$), strontium titanate ($SrTiO_3$), and barium titanate ($BaTiO_3$) are workhorse electroceramic materials. They have various important electrical properties, including reports of relative permittivities of 273 (1 kHz, 500 nm),[1] 475 (100 kHz, 600 nm),[2] and 630 (1 kHz, 380 nm),[3] in thin films. Applications include high charge-density capacitors and dynamic random access memories.[4] Capacitors based on such electroceramics are ubiquitous energy storage devices in electronics applications, for example, in surface-mounted multilayer capacitors and in larger capacitance rolled devices.[5,6]

In most applications, electroceramic materials are prepared by conventional powder processing methods at high temperature. Sol−gel processes are used extensively in silicate processing and find various applications elsewhere, variously providing high purity, mild chemical synthesis conditions, stoichiometric control, homogeneous doping, porosity, and/or high optical quality.[7] There are reports of sol−gel production of perovskite titanate thin films using spin-coating[8−10] or dip-coating,[3,11−13] with sols typically stabilized by acetylacetonate, acetate, and methoxyethanol. Film quality is often not discussed in detail in the literature, but volume contraction of the coating during drying can create internal stresses, which cause cracking and pinholes (cracks that cannot propagate due to the film thickness being lower than the critical stress intensity).[14,15]

Film porosity is a critical factor for the production of dielectric thin films for applications such as capacitive devices. If the film is porous, electrode deposition techniques such as thermal evaporation or sputtered electrodes can result in electrical short circuits. No account is usually taken of porosity when calculating effective permittivity values, and the permittivities measured in standard experiments using solid samples and metal contacts are an average across the film as a whole.[16] There are many methods that have been reported to reduce film porosity, such as the way the films are dried (gaseous environment,[17,18] calcination temperature,[19] and duration[20]), increasing the number of coatings in the film,[21] the addition of dopants,[22] the concentration of water in acid-catalyzed sols,[23] and the aging duration.[24] In many cases, for $BaTiO_3$ thin films, multiple dipping and annealing steps have been employed to fill in porosity in sol−gel $BaTiO_3$ films, and this process allowed electrical properties to be measured.[11] A review of the literature (Supporting Information (SI), Table S1) shows that when $BaTiO_3$ films are made by sol−gel deposition (whether spin- or dip-coating), electrical measurements are only reported on films made with multiple coatings.[3,9−11,16,25−27]

Herein, a sol−gel dip-coating method to produce $BaTiO_3$ thin films on platinum is optimized to remove pinholes and cracks. These single dip films still short circuited when contacted, and multiple dipping steps were used to achieve

Received: January 27, 2018
Accepted: April 25, 2018
Published: June 25, 2018

DOI: 10.1021/acsomega.8b00173
ACS Omega 2018, 3, 6880−6887

solid-state impedance measurements. A new approach using electrochemical impedance in combination with optical and electron microscopy has then been used to improve the understanding of the porosity in the films, allowing the effective permittivity of the $BaTiO_3$ itself to be assessed.

RESULTS AND DISCUSSION

Sol–Gel $BaTiO_3$ Film Optimization. The sol recipe used to produce $BaTiO_3$ films was fairly typical of those in the literature, with coordinating solvents and a reaction moderator (acac) used to stabilize the reactive titanium centers. The films were dipped onto Pt-coated silicon wafers. Grazing incidence X-ray diffraction (XRD) of the films fired at 750, 800, 850, and 900 °C (Figure 1) showed cubic $BaTiO_3$ with lattice

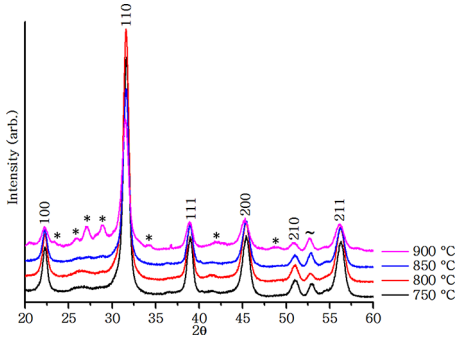

Figure 1. Grazing incidence X-ray diffraction (GIXRD) (1° incident angle) of thin-film $BaTiO_3$ deposited on Si/Pt substrates and annealed at the indicated temperatures. Reflections due to cubic $BaTiO_3$ are marked with Miller indices, (~) indicates Pt signals from the substrate, and (*) is the $Ba_2Ti_{13}O_{22}$ impurity in the 900 °C sample.

parameters of 4.0060(7), 4.0070(6), 4.0057(8), and 4.001(3) Å, respectively. A typical literature value is 4.014 Å.[28] The crystallite sizes were measured using the Halder–Wagner method[29] in PDXL software as 132 ± 11 Å across all temperatures, with no obvious trend with firing temperature. However, at higher annealing temperatures, a $Ba_2Ti_{13}O_{22}$ impurity was also found in the $BaTiO_3$ films, so the work focused on the phase-pure $BaTiO_3$ films, which were annealed at 750 °C.

The initial single dip $BaTiO_3$ films contained a high density of pinholes that became visible by eye during drying of the gels and remained visible after the annealing step. Optical microscopy (Figure 2a) showed some delamination and exposure of the substrate in the center of the pinhole. The delaminated region was shown by scanning electron microscopy (SEM) (Figure 2b) to contain a series of short cracks, which then open up a little due to the film shrinkage during drying. Presumably, these cracks do not propagate across the film thickness as the film thickness is below the critical stress of the material.[14] The energy-dispersive X-ray spectroscopy (EDS) maps showed fairly even composition across the flakes of the material within the pinholes and a 1:1 ratio of Ti to Ba (Figure 2c,d), suggesting that pinhole formation is not due to local composition variations. This is supported by microfocus XRD maps across pinholes, where only $BaTiO_3$ and Pt were observed.

Pinholes are disadvantageous as they can cause electrical shorting and also have a significant influence on capacitance.[30,31] This is because the air void has a relatively low polarizability when compared to the intrinsic properties of the

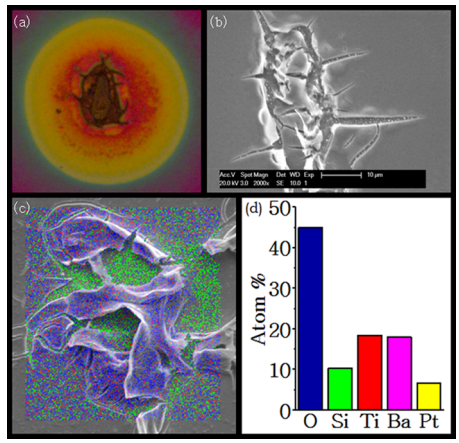

Figure 2. Optical microscopy (a), SEM image (b), colored EDS map (c, blue, green, red, purple, and yellow dots correspond to oxygen, silicon, titanium, barium, and platinum, respectively), and quantification of the EDS map (d, with values reported in SI, Table S2) of the region of a pinhole in an unoptimized single dip $BaTiO_3$ film annealed at 750 °C.

film; therefore, large volume fractions of pinholes will significantly influence the capacitance. Their formation has been attributed to poor substrate cleaning,[32−34] lack of grain coalescence,[35] and solvent effects on the particulate species present within the sol.[36] A number of variations to our glassware and substrate cleaning processes were trialed and had no clear effect on pinhole density. Hence, variants in the sol composition and aging were explored with the aim of reducing pinhole formation.

(1) The amount of water added to the sol formulation to hydrolyze the titanium isopropoxide was varied. After 1 day of aging, the substrate was dipped into the four different sols and then annealed at 750 °C. The film with the lowest number of pinholes (SI, Figure S1) was produced with 4 mL of H_2O, and so this modification was then maintained. The films produced with 4 mL of water contained larger particles than those produced at lower water concentration (optical micrographs in SI, Figure S2); this change has been attributed to the degree of cross-linking and polycondensation occurring over the defined aging period.

(2) The length of the sol aging period is also a vital control parameter as the number and size of oligomers formed within the sol will vary with the amount of time over which hydrolysis and polycondensation occur. As the film aging period gradually increased from 1 to 8 days, the pinhole density gradually fell (SI, Figure S3), with a very low density of pinholes observed with aging periods between 6 and 8 days. With these longer aging periods, the films developed small pores that could be observed under the microscope (distinct from the large pinholes described above that are visible to the naked eye), but also increased in overall density (SI, Figure S2). This is consistent with an increase in sol viscosity.[37] On day 9, the sol had started to gel, and coatings produced from were not smooth or well adhered.

(3) The final modification was to the stirring speed during aging, which was increased from 250 to 1000 rpm. This improved reproducibility of the aging periods, and reduced the period taken to produce sols that did not

DOI: 10.1021/acsomega.8b00173
ACS Omega 2018, 3, 6880−6887

generate pinholes by 2−3 days compared to that at 250 rpm (SI, Figure S3). At this stirring speed, full gelation did not occur even after 9 days, although after 7 days cracks appeared on the film due to high-viscosity sols (SI, Figure S3b).

The faster stirring speed resulted in shorter aging periods to produce pinhole-free films but also reduced the size of the pores that occur in these films (SI, Figure S2). Further films were produced using 4 mL of water and stirred at 1000 rpm for 3−4 days.

Films Produced with Multiple Dippings. Even after the sol synthesis and aging process had been optimized to avoid pinhole formation, attempts at electrical measurements of the single dip $BaTiO_3$ films always failed. Various methods were used to contact the film top surface (evaporated gold, gallium, gallium−indium eutectic), but short circuits to the platinum film substrate were always observed. Hence, even the small pores observed in the microscopy are sufficient for these media to penetrate the film. As noted in the Introduction, multiple dippings have been claimed to fill in the pores and allow electrical measurement,[11] and in all cases where electrical properties have been reported, multiple coating cycles have been employed (SI, Table S1). Hence, films were produced using the optimized dip conditions described above with multiple rounds of dipping and firing. In these films, GIXRD (Figure 3) showed the cubic $BaTiO_3$ to have a constant lattice parameter (4.008 ± 0.003 Å) and crystallite size (160 ± 20 Å); Pt substrate signals were obscured by these thicker films.

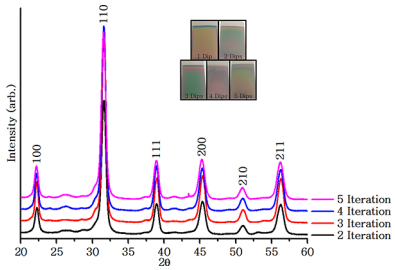

Figure 3. GIXRD (1° incident angle) of $BaTiO_3$ films deposited on Si/Pt substrates and annealed at 750 °C. Reflections due to cubic $BaTiO_3$ are marked with Miller indices. The inset shows photgraphs of the films.

The films were smooth to the eye, but under the optical microscope changes to the microstructure were observed (Figure 4). Over the first three layers of $BaTiO_3$ deposited, the pores became smaller but were more numerous. In layer 4 cracks started to appear, and in layer 5 these had propagated to a network of narrow cracks, leaving ∼5 μm $BaTiO_3$ islands. The film thicknesses progressively increased from 300 nm with 1 dip and anneal cycle, to 550, 600, 930, and 1250 nm with 2, 3, 4, and 5 cycles, respectively. The cross-sectional SEM images (SI, Figure S4) also showed further evidence of the porosity present between the $BaTiO_3$ grains, which did not appear to have been mitigated by the multiple dipping process.

Solid-State Impedance Measurements. Single dip films suffered from short circuits when top contacts were applied due to the metal penetrating through the pores. The most continuous $BaTiO_3$ films produced in this study were with two or three dip and anneal cycles, and with further cycles, cracking of the films started to develop. Solid-state impedance measurements were focused on the films produced with three

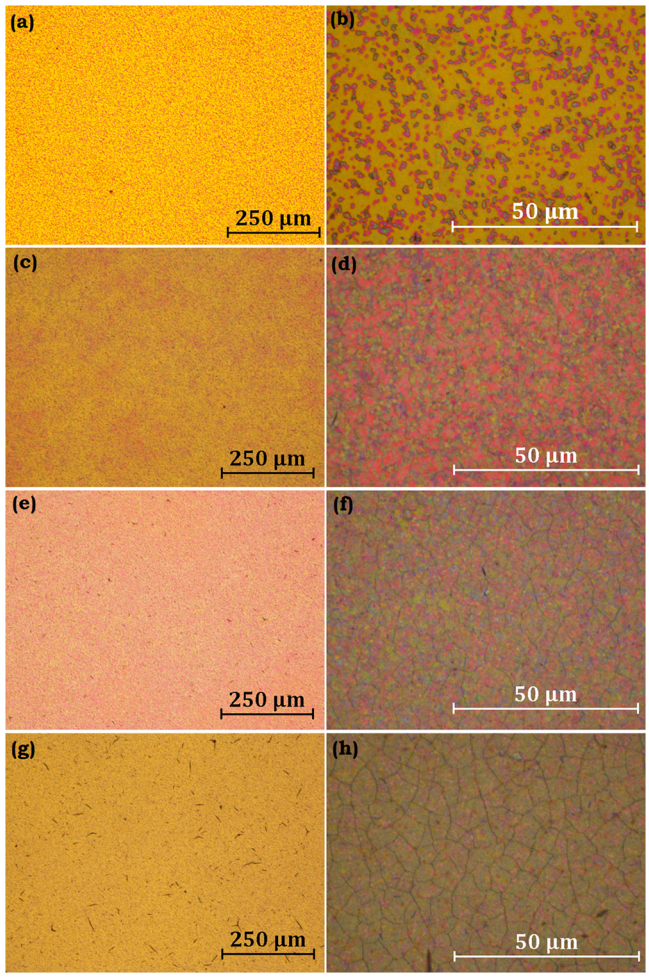

Figure 4. Optical micrographs (left 10×, right 100×) of $BaTiO_3$ films produced using multiple dip and anneal (750 °C) cycles: (a, b) 2 layers; (c, d) 3 layers; (e, f) 4 layers; (g, h) 5 layers.

coating cycles. Gold was evaporated onto the surface of one of these films using a mask with multiple contact diameters (0.420, 0.515, and 0.615 mm; SI, Figure S5). The gold contacts were used as the top contact and the Pt film as the bottom contact. Impedance spectroscopy was then carried out with a frequency range of 1 MHz to 100 Hz and a sinusoidal amplitude of 500 mV on three gold pads of each size. The Nyquist and Bode plots (Figure 5) show a capacitive response consistent with an equivalent circuit of a resistor and a constant phase element (CPE) in series; this equivalent circuit was used to fit all of the solid-state data. The phase angle was just below 90° throughout the frequency range, the modulus gradient was −0.99, and the magnitude of the capacitance was scaled accordingly with the pad area. CPE components are often used to model non-ideal capacitance (e.g., inhomogeneities),[38] but note that the modulus gradient close to −1 indicates that the capacitance measured here was close to ideal over the modeled frequency range. The electrical response was highly reproducible across each pad area, with the electrical noise reducing with increasing pad area. Using the parallel plate equation ($C = A\varepsilon\varepsilon_0/d$, where C is capacitance in F, A is pad area in m^2, ε_0 is the permittivity of free space in m^{-3} kg^{-1} s^4 A^2, ε is the effective permittivity of the film, and d is its thickness in meters), the effective permittivity of the films in each of these regions was then calculated. These were remarkably consistent (SI, Table

DOI: 10.1021/acsomega.8b00173
ACS Omega 2018, 3, 6880−6887

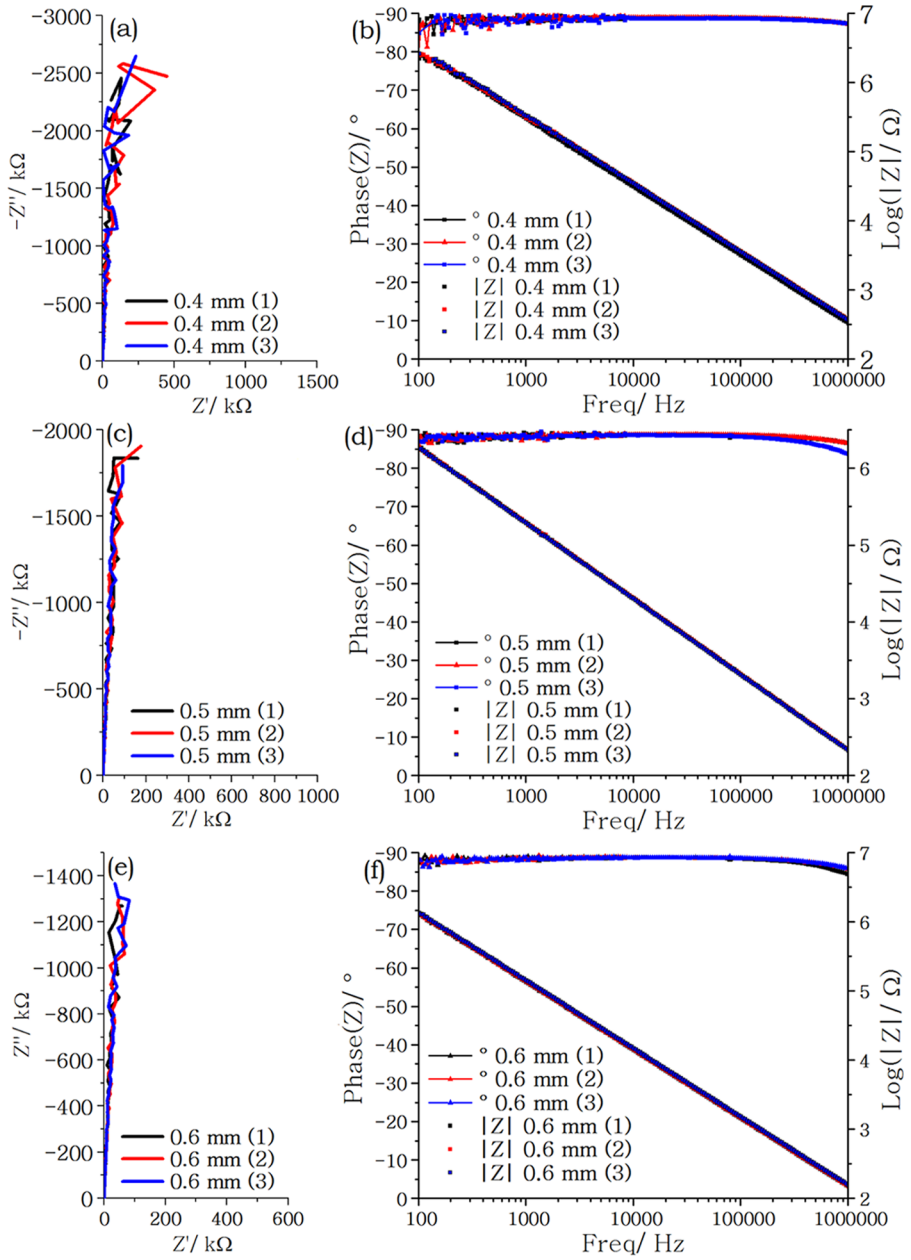

Figure 5. Nyquist (left) and Bode (right) plots of the solid-state impedance data for a $BaTiO_3$ thin film produced by dipping and annealing at 750 °C three times: (a, b) 0.4 mm; (c, d) 0.5 mm; (e, f) 0.6 mm diameter contact areas. Each experiment was performed on three gold pads of the same diameter to confirm reproducibility (the fittings are shown in SI, Figures S7–S9).

S3), with an average value of 290 and all solid-state measurements resulting in effective permittivities between 270 and 299 (data fitted in the range 500 Hz to 1 MHz). Capacitance and effective permittivity both decreased gradually with increasing applied frequency (SI, Figure S6 and Table S4).

Electrochemical Impedance Measurements. Multiple sol–gel coating cycles have previously been reported to fill in the pores in $BaTiO_3$ films and hence allow the solid-state impedance to be measured.[11] However, Figure 4 indicates that some porosity is present even in the films that have been coated multiple times. Cyclic voltammograms of films produced with 1, 2, or 3 dip and anneal cycles in acid electrolyte (Figure 6) all showed the same features typical of platinum electrochemistry. Figure 6 shows characteristic hydrogen adsorption (H_{ads}) and hydrogen desorption (H_{des}) peaks in the potential range between −0.6 and −0.4 V.[39] The current densities of these features are enhanced by coating with the porous film, which can be attributed to the effect of the pore structure[40] and to the thermal processing close to the platinum Tammann temperature.[41]

An electrochemical impedance study was undertaken in 0.5 M K_2SO_4 at 0 V versus $Hg/HgSO_4$ (cyclic voltammogram available SI, Figure S10) with the aim of ascertaining how large an effect the porosity has on the capacitance. A comparison between the Pt film substrate and the substrate with a $BaTiO_3$ thin film produced with a single dip and anneal cycle is shown in Figure 7. Unsurprisingly, the bare substrate shows a much lower charge transfer resistance (smaller semicircle in the area normalized Nyquist plot) than that of the resistive $BaTiO_3$ film. The Bode plots (Figure 7) show purely resistive behavior at high frequencies due to the solution resistance and mainly capacitive behavior from 0.1 to 1000 Hz. At low frequency, the

DOI: 10.1021/acsomega.8b00173
ACS Omega 2018, 3, 6880–6887

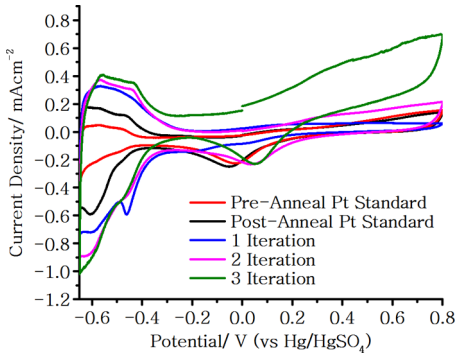

Figure 6. Cyclic voltammograms of $BaTiO_3$ thin films produced on a Si/Pt substrate with 1, 2, or 3 cycles of dipping into a sol followed by firing at 750 °C and of a blank Si/Pt substrate pre- and postannealed. 1 cm × 1 cm regions were defined using nail polish; the scan rate was 100 mV s^{-1}. A Pt gauze counter electrode and a $Hg/HgSO_4$ reference electrode were used with a nonaerated 1 mol dm^{-3} H_2SO_4 electrolyte.

response goes back to a resistive behavior modeling the film resistance and the solution resistance. The Bode plots for the bare substrate and the film are almost identical, with only a shift along the frequency axis resulting from the resistive component of the $BaTiO_3$ film.

A porous dielectric film is expected to exhibit two parallel impedances associated with transport through the dielectric and the pores. The dielectric part is expected to contain parallel dielectric capacitance and resistance components, whereas the pores should exhibit a double-layer capacitance from the platinum surface in series with a pore resistance (SI, Figure S11). A series of films that had been dipped and annealed between 1 and 5 times were studied with different areas of the film exposed to the electrolyte. Nyquist and Bode plots for a series of samples with nominally increasing deposit thicknesses are shown in SI, Figure S12. The Nyquist plots only show partial arcs from near the origin to the low-frequency parallel resistance, scaling inversely with the sample area. The Bode plots all show a linear slope of −0.95 in modulus and a constant phase angle of around 85° from about 1 Hz to 1 kHz, signifying a capacitance $(-1/2\pi fZ'')$ on the order of 100 μF and scaling with the sample area. At frequencies below 1 Hz, a lowering of both the phase angle and modulus suggests a parallel "leakage" resistance in the range of MΩ, which can be attributed to the redox behavior of impurities such as oxygen in solution. At frequencies higher than 100 Hz, the phase angle decreases to almost 0, coinciding with a leveling off of the impedance to constant values of just a few ohms. The latter value corresponds well to the estimated series resistance of the electrolyte.

We conclude that the effects of a complex porosity prevent a resolution of the capacitance into C_{dl} and C_D, and the equivalent circuit is effectively reduced to that shown in Figure 7, where the capacitances are effectively placed in parallel across the same leakage resistor, and the solution resistance is in series with all other components. The data are provided in SI, Figure S12, with fits shown in SI, Figures S13−S17, and the fitted parameters in SI, Table S5. The CPE in this case was used to account for the depression of the semicircle, which can be attributed to the energetic heterogeneity due to the random geometric distribution of the two capacitances.[42] An alternative approach to fit the data is the use of random $R-C$ networks.[43,44] Capacitance values varied between 6 and 11 μF cm^{-2}, with similar values throughout and no obvious trend in the values (Figure 8). An obvious conclusion from these data is that the exposed Pt surface area is similar in all films and hence pores are not filled in during multiple coating cycles. The ability to measure solid-state impedance on such samples must

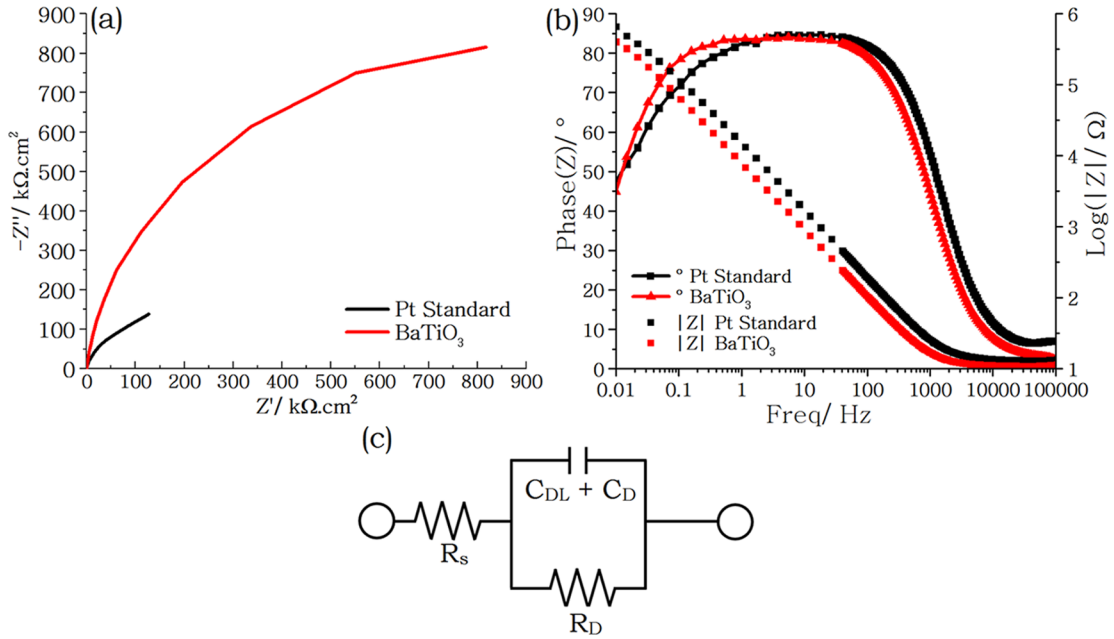

Figure 7. Nyquist (left) and Bode (right) plots of the electrochemical impedance data for a Pt film substrate and a $BaTiO_3$ thin film produced by dipping and annealing at 750 °C. Data were collected in 0.5 mol dm^{-3} K_2SO_4 (20 mL) with a Pt gauze counter electrode and a $Hg/HgSO_4$ (sat. K_2SO_4) reference electrode. A sinusoidal potential with 10 mV amplitude was applied at frequencies from 0.1 MHz to 10 mHz. (a) Nyquist plot using data normalized to the exposed surface area of the substrate or film, (b) Bode plot without this normalization, and (c) equivalent circuit used in data fitting, where R_s is uncompensated solution resistance, C_{dl} is double-layer capacitance, C_D is dielectric capacitance, and R_D is dielectric resistance (pore resistance was discounted).

DOI: 10.1021/acsomega.8b00173
ACS Omega 2018, 3, 6880−6887

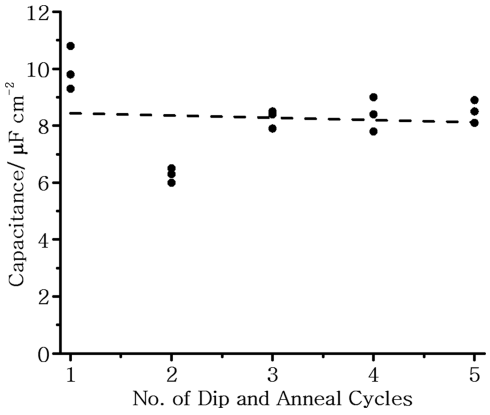

Figure 8. Variation in area normalized capacitance of $BaTiO_3$ films produced by dipping and annealing at 750 °C 1−5 times and each measured using three different areas exposed to the electrolyte. The broken line is a guide to the eye.

be due to increasing thickness of the films and increasing tortuosity of the pores, resulting in a lower tendency for the evaporated gold, or other contact material, to penetrate to the substrate surface.

DISCUSSION

The effective permittivity of the $BaTiO_3$ films of 290 that was derived from the solid-state impedance is significantly higher than that of air (effective permittivity = 1), and so it is reasonable to assume that the pores in the films contribute a negligible amount to the measured capacitance. The Pt double-layer capacitance determined by fitting the data in Figure 7 was 34.8 μF cm^{-2}, significantly higher than the overall film capacitance determined from Figure 5 of 0.43 μF cm^{-2}. The capacitance of the $BaTiO_3$ films measured by electrochemical impedance spectroscopy, of ∼8 μF cm^{-2}, shows a mixture of Pt double-layer capacitance due to electrolyte ingress through the pores and capacitance due to the $BaTiO_3$ film. Considering both types of impedance data together, it is possible to evaluate the relative contributions of these two capacitances in the electrochemical impedance and hence to delineate the effect of the porosity on the effective permittivity of the films.

For the three dip films, where we have overall film capacitance data from the solid-state impedance, subtracting the overall film capacitance (0.43 μF cm^{-2}) from the electrochemical capacitance (8.26 μF cm^{-2}) provides a double-layer capacitance contribution of 7.83 μF cm^{-2}. Dividing this value by the Pt double-layer capacitance of a bare Pt film (34.8 μF cm^{-2}) yields an overall pore area of 22.5% of the film surface. This means that the $BaTiO_3$ measured in the solid-state impedance only covered 77.5% of the surface and the effective permittivity of the $BaTiO_3$ itself is higher than that of the film overall, with a value of around 374. Hence, if sol−gel coating processes could be refined to avoid all porosities, an increase in permittivity of the films of around 29% would be feasible.

CONCLUSIONS

Sol−gel $BaTiO_3$ films have been optimized to minimize cracks and pinholes by modifying the water content, aging time, and stirring speed during aging. The resultant films are optically smooth and continuous, but do have a significant degree of porosity. After multiple cycles of coating and annealing, it was possible to measure the overall film permittivity. These films were found to retain significant porosity, and electrochemical impedance spectroscopy was demonstrated to be a useful technique in such systems to probe the impedance associated with both the pores and the film material. This approach could be powerful in evaluating the effect of porosity on the properties of electroceramic films and in optimizing deposition processes to minimize porosity effects.

EXPERIMENTAL SECTION

All of the reagents were used without further purification. 2-Methoxyethanol (99.8%), acetylacetonate (>99%), titanium isopropoxide (97%), and barium acetate (99%) were purchased from Sigma-Aldrich and used as received. Glacial acetic acid (>99%) and potassium sulfate (99%) were purchased from Fisher Scientific. Deionized water was produced with a Purelab Options, ELGA LA620 deionizer.

The preparation of $BaTiO_3$ precursor sols was based on a previous report (SI, Figure S18).[13] $Ti(O^iPr)_4$ (2.618 g, 9.21 mmol) was added to a mixture of methoxyethanol (23.505 g, 309 mmol) and acetylacetone (1.508 g, 15.6 mmol) under N_2 in a dry bottle. In a separate bottle, $Ba(OAc)_2$ (2.353 g, 9.21 mmol) was dissolved by stirring in concentrated acetic acid (15 mL, 262 mmol); then, H_2O (1−4 mL, 55.5−222 mmol) was added. The $Ba(OAc)_2$ solution was added dropwise to the $Ti(O^iPr)_4$ solution under a N_2 flow. The sol was then sealed in the bottle and allowed to stir at 250 or 1000 rpm over periods ranging from 1 to 14 days depending on water and acetic acid contents.

Sols were deposited onto dry 90 nm Pt-coated Si(100) substrates (20 mm × 30 mm; Ti adhesion layer; ECS Partners Southampton, cleaned by sonicating for 15 min each in acetone, ethanol, isopropyl alcohol, and deionized water). Substrates were dipped into the sol at a 30 mm s^{-1} immersion speed, held for 30 s, and then withdrawn at 40 mm s^{-1} and left to dry for 10 min (NIMA Technology 5.20 dip-coater). The films were then placed into a crucible and fired at 750 °C for 40 min (ramp rate of 1 °C min^{-1} and cooling at 5 °C min^{-1}).

Grazing incidence X-ray diffraction was collected using a Rigaku Smartlab diffractometer with a parallel beam of Cu K_α X-rays, incident angle of 1°, and a DTex250 1D detector. Rietveld refinement was carried out using the Rigaku PDXL2 package. Scanning electron microscopy (SEM) and energy-dispersive X-ray spectrometry (EDS) were performed on a JEOL JSM6500F microscope with an Oxford Instruments INCA x-sights EDS/EDX detector. Optical images were taken on a Nikon Eclipse optical microscope.

Solid-state impedance measurements were performed with an Agilent 4294A Precision Impedance Analyser. Gold top electrodes of various diameters (0.4, 0.5, and 0.6 mm) were evaporated onto the $BaTiO_3$ thin film. The Pt of the Si/Pt/$BaTiO_3$ substrate was then contacted as the working electrode. The sinusoidal potential amplitude was 500 mV, and the measurement frequency was from 1 MHz to 100 Hz. Data were fitted with ZView (Scribner Associates Inc).

Electrochemical impedance measurements were carried out using a Biologics SP-150 potentiostat. An area of the $BaTiO_3$ thin film was defined by masking the surrounding area and film edges with an insulating medium (nail polish). The $BaTiO_3$ thin-film working electrode was then submerged into 0.5 mol dm^{-3} K_2SO_4 (20 mL) with a Pt gauze counter electrode and a $Hg/HgSO_4$ (sat. K_2SO_4) reference electrode. A sinusoidal potential of 0 V versus $Hg/HgSO_4$ with 10 mV amplitude was

DOI: 10.1021/acsomega.8b00173
ACS Omega 2018, 3, 6880−6887

applied at frequencies from 1 MHz to 10 mHz. The subsequent Nyquist plots were fitted using ZView to an appropriate equivalent circuit model giving the capacitance and resistance values.

■ ASSOCIATED CONTENT

Supporting Information

The Supporting Information is available free of charge on the ACS Publications website at DOI: 10.1021/acsomega.8b00173.

Full literature survey of sol−gel-derived $BaTiO_3$ studies, further microscopy and EDX data, further electrical data and derived parameters (PDF)

Raw data for all figures (ZIP)

■ AUTHOR INFORMATION

Corresponding Author

*E-mail: A.L.Hector@soton.ac.uk.

ORCID

Andrew L. Hector: 0000-0002-9964-2163

Gillian Reid: 0000-0001-5349-3468

Author Contributions

Most experiments were conducted by J.W. The research was instigated by A.L.H., C.K., and G.R. who also provided guidance and discussion during the research. J.R.O. provided guidance in the fitting and interpretation of the electrochemical impedance data. The manuscript was written with contributions from all authors, and all approved the final version of the manuscript.

Notes

The authors declare no competing financial interest.

■ ACKNOWLEDGMENTS

The authors thank EPSRC for a CASE award to J.W. (EP/M508147/1) and for funding the Smartlab diffractometer (EP/K00509X/1 and EP/K009877/1).

■ REFERENCES

(1) Lian, L.; Sottos, N. R. Effects of Thickness on the Piezoelectric and Dielectric Properties of Lead Zirconate Titanate Thin Films. *J. Appl. Phys.* **2000**, *87*, 3941−3949.

(2) Pontes, F. M.; Lee, E. J. H.; Leite, E. R.; Longo, E.; Varela, J. A. High Dielectric Constant of $SrTiO_3$ Thin Films. *J. Mater. Sci.* **2000**, *35*, 4783−4787.

(3) Kumazawa, H.; Masuda, K. Fabrication of Barium Titanate Thin Films with a High Dielectric Constant by a Sol-gel Technique. *Thin Solid Films* **1999**, *353*, 144−148.

(4) Basceri, C.; Streiffer, S. K.; Kingon, A. I.; Waser, R. The Dielectric Response as a Function of Temperature and Film Thickness of Fiber-Textured (Ba,Sr)TiO_3 Thin Films Grown by Chemical Vapor Deposition. *J. Appl. Phys.* **1997**, *82*, 2497−2504.

(5) Guo, Y.; Batra, S.; Chen, Y.; Wang, E.; Cakmak, M. Roll to Roll Electric Field "Z" Alignment of Nanoparticles from Polymer Solutions for Manufacturing Multifunctional Capacitor Films. *ACS Appl. Mater. Interfaces* **2016**, *8*, 18471−18480.

(6) Brennecka, G. L.; Ihlefeld, J. F.; Maria, J. P.; Tuttle, B. A.; Clem, P. G. Processing Technologies for High-Permittivity Thin Films in Capacitor Applications. *J. Am. Ceram. Soc.* **2010**, *93*, 3935−3954.

(7) Blum, J. B.; Gurkovich, S. R. Sol-Gel-Derived $PbTiO_3$. *J. Mater. Sci.* **1985**, *20*, 4479−4483.

(8) Adikary, S.; Chan, H. L. Ferroelectric and Dielectric Properties of Sol-gel Derived $Ba_xSr_{1-x}TiO_3$ Thin Films. *Thin Solid Films* **2003**, *424*, 70−74.

(9) Sharma, H. B.; Mansingh, A. Phase Transition in Sol-Gel-Derived Barium Titanate Thin Films. *J. Phys. D: Appl. Phys.* **1998**, *31*, 1527−1533.

(10) Lee, B.; Zhang, J. Preparation, Structure Evolution and Dielectric Properties of $BaTiO_3$ Thin Films and Powders by an Aqueous Sol-gel Process. *Thin Solid Films* **2001**, *388*, 107−113.

(11) Hayashi, T.; Ohji, N.; Hirohara, K.; Fukunaga, T.; Maiwa, H. Preparation and Properties of Ferroelectric $BaTiO_3$ Thin Films by Sol-Gel Process. *Jpn. J. Appl. Phys.* **1993**, *32*, 4092−4094.

(12) Mahmoodi, N.; Vaezi, M. R.; Kazemzadeh, A. Preparation of Stable Sol and Free-Cracks Thin Film of Barium Titanate via Sol-Gel Dip Coating Method. *J. Ceram. Process. Res.* **2014**, *15*, 312−315.

(13) Al-Arjan, W. S.; Algaradah, M. M. F.; Brewer, J.; Hector, A. L. Sol-gel Preparation of Well-Adhered Films and Long Range Ordered Inverse Opal Films of $BaTiO_3$ and $Bi_2Ti_2O_7$. *Mater. Res. Bull.* **2016**, *74*, 234−240.

(14) Thouless, M. D. Decohesion of Films with Axisymmetric Geometries. *Acta Metall.* **1988**, *36*, 3131−3135.

(15) Wang, D.; Bierwagen, G. P. Sol-Gel Coatings on Metals for Corrosion Protection. *Prog. Org. Coat.* **2009**, *64*, 327−338.

(16) Kamalasanan, M. N.; Kumar, N. D.; Chandra, S. Dielectric and Ferroelectric Properties of $BaTiO_3$ Thin Films Grown by the Sol-Gel Process. *J. Appl. Phys.* **1993**, *74*, 5679−5686.

(17) Brinker, J.; Scherer, G. *Sol-Gel Science: The Physics and Chemistry of Sol-Gel Processing*, 1st ed.; Academic Press, 1990; pp. 1−912.

(18) Ashiri, R.; Nemati, A.; Sasani Ghamsari, M. Crack-Free Nanostructured $BaTiO_3$ thin Films Prepared by Sol-Gel Dip-Coating Technique. *Ceram. Int.* **2014**, *40*, 8613−8619.

(19) Lee, H. J.; Hahn, S. H.; Kim, E. J.; You, Y. Z. Influence of Calcination Temperature on Structural and Optical Properties of TiO_2-SiO_2 Thin Films Prepared by Sol-Gel Dip Coating. *J. Mater. Sci.* **2004**, *39*, 3683−3688.

(20) Arconada, N.; Durán, A.; Suárez, S.; Portela, R.; Coronado, J. M.; Sánchez, B.; Castro, Y. Synthesis and Photocatalytic Properties of Dense and Porous TiO_2-Anatase Thin Films Prepared by Sol-gel. *Appl. Catal., B* **2009**, *86*, 1−7.

(21) Ghodsi, F.; Tepehan, F.; Tepehan, G. Optical and Electrochromic Properties of Sol-gel Made CeO_2-TiO_2 Thin Films. *Electrochim. Acta* **1999**, *44*, 3127−3136.

(22) Chauhan, P.; Annapoorni, S.; Trikha, S. K. Humidity-Sensing Properties of Nanocrystalline Haematite Thin Films Prepared by Sol-Gel Processing. *Thin Solid Films* **1999**, *346*, 266−268.

(23) Fardad, M. A.; Yeatman, E. M.; Dawnay, E. J. C.; Green, M.; Horowitz, F. Effects of H_2O on Structure of Acid-Catalysed SiO_2 Sol-Gel Films. *J. Non-Cryst. Solids* **1995**, *183*, 260−267.

(24) Chen, D. Anti-Reflection (AR) Coatings Made by Sol-gel Processes: A Review. *Sol. Energy Mater. Sol. Cells* **2001**, *68*, 313−336.

(25) Huang, L.; Chen, Z.; Wilson, J. D.; Banerjee, S.; Robinson, R. D.; Herman, I. P.; Laibowitz, R.; O'Brien, S. Barium Titanate Nanocrystals and Nanocrystal Thin Films: Synthesis, Ferroelectricity, and Dielectric Properties. *J. Appl. Phys.* **2006**, *100*, No. 034316.

(26) Hayashi, T.; Oji, N.; Maiwa, H. Film Thickness Dependence of Dielectric Properties of $BaTiO_3$ Thin Films Prepared by Sol-Gel Method. *Jpn. J. Appl. Phys.* **1994**, *33*, 5277−5280.

(27) Basantakumar Sharma, H.; Sarma, H. N. K.; Mansingh, A. Ferroelectric and Dielectric Properties of Sol-Gel Processed Barium Titanate Ceramics and Thin Films. *J. Mater. Sci.* **1999**, *34*, 1385−1390.

(28) Yen, F.-S.; Hsiang, H.-I.; Chang, Y.-H. Cubic to Tetragonal Phase Transformation of Ultrafine $BaTiO_3$ Crystallites at Room Temperature. *Jpn. J. Appl. Phys.* **1995**, *34*, 6149−6155.

(29) Halder, N. C.; Wagner, C. N. J. Separation of Particle Size and Lattice Strain in Integral Breadth Measurements. *Acta Crystallogr.* **1966**, *20*, 312−313.

(30) van de Krol, R. Mott-Schottky Analysis of Nanometer-Scale Thin-Film Anatase TiO_2. *J. Electrochem. Soc.* **1997**, *144*, 1723−1727.

(31) Xu, M.; Feng, J.; Ou, X.-L.; Zhang, Z.-Y.; Zhang, Y.-F.; Wang, H.-Y.; Sun, H.-B. Surface Passivation of Perovskite Film by Small Molecule Infiltration for Improved Efficiency of Perovskite Solar Cells. *IEEE Photonics J.* **2016**, *8*, 1−7.

DOI: 10.1021/acsomega.8b00173
ACS Omega 2018, 3, 6880−6887

(32) Lee, H.-C.; Park, O. O. Round Pinholes in Indium-Tin-Oxide Thin Films on the Glass Substrates: A Taguchi Method Analysis and Theoretical Approach to Their Origins. *Vacuum* **2004**, *72*, 411−418.
(33) Lisco, F.; Abbas, A.; Maniscalco, B.; Kaminski, P. M.; Losurdo, M.; Bass, K.; Claudio, G.; Walls, J. M. Pinhole Free Thin Film CdS Deposited by Chemical Bath Using a Substrate Reactive Plasma Treatment. *J. Renewable Sustainable Energy* **2014**, *6*, No. 011202.
(34) Lee, S. M.; Cahill, D. G. Heat Transport in Thin Dielectric Films. *J. Appl. Phys.* **1997**, *81*, 2590−2595.
(35) Tashkandi, M. A.; Sampath, W. S. In *Morphology of CdS Thin Films: Pinholes and Their Effect on Open Circuit Voltage in CdS/CdTe Solar Cells*, 37th IEEE Photovoltaic Specialists Conference; IEEE, 2011; pp. 001700−001704.
(36) Chen, H.-S.; Kumar, R. V. Sol-gel TiO_2 in Self-Organization Process: Growth, Ripening and Sintering. *RSC Adv.* **2012**, *2*, 2294−2301.
(37) Cairncross, R. A.; Schunk, P.; Chen, K. S.; Prakash, S. S.; Samuel, J.; Hurd, A.; Brinker, C. J. Pore Evolution and Solvent Transport During Drying of Gelled Sol-Gel Coatings: Predicting "Springback.". *Drying Technol.* **1997**, *15*, 1815−1825.
(38) Evgenij, B.; Macdonald, J. *Impedance Spectroscopy Theory, Experiment, and Applications*, 2nd ed.; John Wiley & Sons, Inc.: New Jersey, 2005; pp. 1−595.
(39) Daubinger, P.; Kieninger, J.; Unmüssig, T.; Urban, G. A. Electrochemical Characteristics of Nanostructured Platinum Electrodes -a Cyclic Voltammetry Study. *Phys. Chem. Chem. Phys.* **2014**, *16*, 8392−8399.
(40) Walcarius, A.; Sibottier, E.; Etienne, M.; Ghanbaja, J. Electrochemically Assisted Self-Assembly of Mesoporous Silica Thin Films. *Nat. Mater.* **2007**, *6*, 602−608.
(41) Golunski, S. E. Why Use Platinum in Catalytic Converters? *Platinum Met. Rev.* **2007**, *51*, 162.
(42) Córdoba-Torres, P.; Mesquita, T. J.; Nogueira, R. P. Relationship between the Origin of Constant-Phase Element Behavior in Electrochemical Impedance Spectroscopy and Electrode Surface Structure. *J. Phys. Chem. C* **2015**, *119*, 4136−4147.
(43) Almond, D. P.; Bowen, C. R. Anomalous Power Law Dispersions in Ac Conductivity and Permittivity Shown to Be Characteristics of Microstructural Electrical Networks. *Phys. Rev. Lett.* **2004**, *92*, No. 157601.
(44) Bouamrane, R.; Almond, D. P. The Emergent Scaling Phenomenon and the Dielectric Properties of Random Resistor-capacitor Networks. *J. Phys.: Condens. Matter* **2003**, *15*, 4089−4100.

DOI: 10.1021/acsomega.8b00173
ACS Omega 2018, 3, 6880−6887